JOURNAL OF THERMOPHYSICS AND HEAT TRANSFER
Vol. 23, No. 3, July–September 2009

Spectroscopic Observation of Translational–Rotational Nonequilibrium in Low-Density Hydrogen Plasma Flow

Yoshiki Takama* and Kojiro Suzuki†
University of Tokyo, Kashiwa, Chiba 277-8561, Japan

DOI: 10.2514/1.41805

Translational–rotational nonequilibrium of low-density hydrogen plasma flow was investigated using emission spectroscopy. The translational temperature can be determined by Balmer H_β line profile fitting, taking into account instrumental broadening, Doppler broadening, and spin-orbit coupling, when natural, Stark, and Zeeman broadenings are less dominant. The rotational temperature can be determined by the line intensity fitting of the Fulcher-α band. This emission spectroscopic method was experimentally applied to our low-density inductively coupled plasma wind tunnel. Spectroscopic measurements of the flow behind the shock wave over a blunt body were conducted. The Knudsen number was on the order of 0.1, and the translational–rotational relaxation time was larger than the flow characteristic time. The nonequilibrium between the translational and rotational modes was successfully observed using our spectroscopic method. The experimental results qualitatively agreed with numerical simulation results.

Nomenclature

A = transition probability, s^{-1}
B = magnetic field flux density, T
C = excitation rate coefficient by electron impact, m^3/s
c = speed of light, 2.998×10^8 m/s
g = Lande g factor
h = Planck constant, 6.626×10^{-34} Js
I = emission intensity, J/m^3
J = rotational quantum number
j = quantum number for the total electronic angular momentum
k_d = forward rate coefficient for the dissociation of a hydrogen molecule, m^3/s
k_{i1} = forward rate coefficient for the ionization of a hydrogen atom, m^3/s
k_{i2} = forward rate coefficient for the ionization of an argon atom, m^3/s
l = azimuthal quantum number
M = molecular weight, g/mol
m = magnetic quantum number
N = number density, m^{-3}
N_e = electron number density, m^{-3}
n = main quantum number
r = radial coordinate, mm
s = spin quantum number
T_e = electron temperature, K
T_{rot} = rotational temperature, K
T_{tra} = translational temperature, K
T_{vib} = vibrational temperature, K
u = velocity, m/s
v = vibrational quantum number
x = axial coordinate, mm
Z_r = translational–rotational relaxation collision number
γ = specific heat ratio
λ = wavelength, nm
μ_0 = permeability of vacuum, 1.257×10^{-6} H/m
μ_B = Bohr magneton, 9.274×10^{-24} J/T
ν = frequency, s^{-1}
τ_f = flow characteristic time, s
τ_r = translational–rotational relaxation time, s

I. Introduction

IN NONEQUILIBRIUM plasmas, the translational, rotational, vibrational, electronic excitation, and electron temperatures have different values. Because the energies in these internal modes are exchanged by collisions of particles to reach the equilibrium state, the extent of nonequilibrium depends on the collision frequency and on the collision number required to equilibrate a particular energy mode. Each internal energy mode has a different collision number. In general, translational and rotational modes rapidly reach equilibrium, whereas vibrational and electronic excitation modes equilibrate slowly with translational mode [1–3]. Therefore, one approach to describe nonequilibrium plasma is the two-temperature model [4], in which the plasma state is approximated by the translational and vibrational temperatures, rotational temperature is assumed to be equal to translational temperature, and electronic excitation temperature and electron temperature are assumed to be equal to vibrational temperature.

Hydrogen molecules are known as a gas that exhibits strong thermal nonequilibrium [5] due to their high characteristic temperatures of rotation and vibration. The translational–rotational relaxation collision number Z_r of hydrogen molecules is reportedly around 200–400 up to 2000 K [6–8], whereas the Z_r of molecules such as nitrogen and oxygen molecules is less than 10 [3,9]. Therefore, for hydrogen molecules, care must be taken before assuming equilibrium between translational and rotational modes in the framework of the two-temperature model. Separately measuring translational and rotational temperatures of hydrogen plasma is necessary considering the nonequilibrium phenomena behind strong shock waves. Such measurement is also necessary when determining the enthalpy of the flow in translational–rotational nonequilibrium in a plasma wind tunnel. Therefore, a diagnostic method for the translational–rotational relaxation of hydrogen molecules needs to be established.

Experimentally, nonequilibrium can be investigated by measuring the temperature corresponding to each internal energy mode. Emission spectroscopy is a widely used effective technique to obtain these plasma temperatures, because it is simple, easy, and nonintrusive. Each plasma temperature is then determined by different

---

Received 25 October 2008; revision received 12 March 2009; accepted for publication 11 April 2009.

*Graduate Student, Japan Society for the Promotion of Science Research Fellow, Department of Advanced Energy, The University of Tokyo, 5-1-5 Kashiwanoha; currently Researcher, Japan Aerospace Exploration Agency; takama@daedalus.k.u-tokyo.ac.jp. Student Member AIAA.

†Professor, Department of Advanced Energy, 5-1-5 Kashiwanoha; kjsuzuki@k.u-tokyo.ac.jp. Member AIAA.

methods of emission spectroscopy. For example, rotational and vibrational temperatures can be determined by spectral fitting of molecular bands [10,11] or by using a Boltzmann plot of particular parts of molecular bands [12–14]. Electronic excitation temperatures of atoms can be determined using a Boltzmann plot. However, measuring the translational temperature by emission spectroscopy is difficult, although measuring the Doppler broadening of an emitted line permits the determination of translational temperature theoretically. This is because accurately estimating the effects of the other broadening mechanisms and extracting the contribution of Doppler broadening is difficult. Determining translational temperature by Doppler broadening requires careful treatment.

In our current study, both translational and rotational temperatures of weakly ionized hydrogen plasmas were determined using emission spectroscopy. The plasmas in the present study consisted of H_2, H, H^+, and e^-. The translational temperature of hydrogen atoms was measured using Doppler broadening of the Balmer H_β line. The effects of the other broadening mechanisms were estimated using the experimental condition and separated into dominant and nondominant factors. As a result, the translational temperature was then determined by line profile fitting of the H_β line, taking into account instrumental broadening, Doppler broadening, and spin-orbit coupling. The applicable range of this emission spectroscopic method to determine translational temperature was also discussed in this study. The rotational temperature of hydrogen molecules was measured using the Fulcher-α band line intensity fitting method that we previously developed [15]. Assuming the presence of a unique translational temperature for the gas mixture, in this current study, we experimentally investigated the translational–rotational nonequilibrium in hydrogen plasma flow. Thus, both translational and rotational temperatures were determined using emission spectroscopy. The establishment of the emission spectroscopic method can contribute to simple nonintrusive diagnosis of the relaxation processes in hydrogen plasma flows. The characteristics of the emission of plasmas can possibly be used to investigate the structure of a rarefied shock layer, which is an area where experimental data are scarce [16,17].

The objectives of this study were to 1) present the emission spectroscopic method to investigate translational–rotational nonequilibrium in hydrogen plasmas, 2) show the applicable range of this method, and 3) apply this method to an actual hydrogen plasma flow and then compare the results with existing relaxation models and numerical simulation. The outline of this paper is as follows. Section II briefly describes the method to determine the rotational temperature. Section III describes the evaluation of H_β line broadening and the method to determine the translational temperature. Section IV describes the experimental apparatus and condition used in our emission spectroscopic method. Section V presents and discusses the experimental results. Section VI summarizes the results and conclusions of this study.

II. Rotational Temperature Determination Method

The rotational temperature of hydrogen molecules was determined by spectral line intensity fitting of the Fulcher-α band of hydrogen molecules [15]. The measured Fulcher-α band spectra are shown in Fig. 1. From this measured band spectra, we selected the lines that had high emission intensity and no interference from other lines. The T_{rot} was then determined by fitting the intensities of these eight lines.

The emission intensity can be written as

$$I^{v',J'}_{v'',J''} = h\nu^{v',J'}_{v'',J''} A^{v',J'}_{v'',J''} N_{v',J'} \tag{1}$$

where single and double primes denote Fulcher upper and lower states, respectively. Assuming corona equilibrium, in which the excitation path is only electron impact from the ground state and the deexcitation path is only radiation to the Fulcher lower state, the population at the Fulcher upper state is described by

$$N_e \sum_{v,J} N_{v,J} C^{v',J'}_{v,J} = N_{v',J'} \sum_{v'',J''} A^{v',J'}_{v'',J''} \tag{2}$$

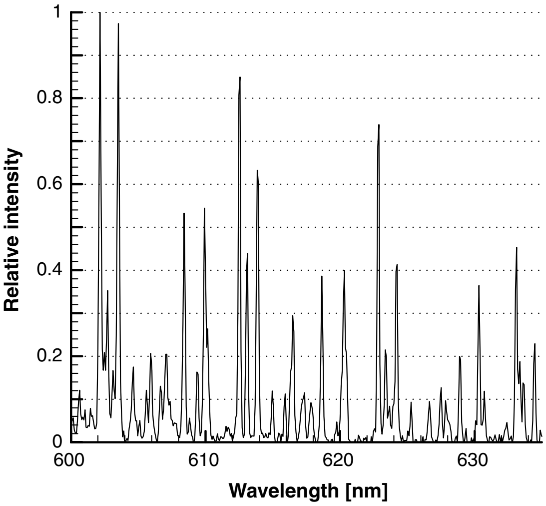

Fig. 1 Fulcher-α band spectra.

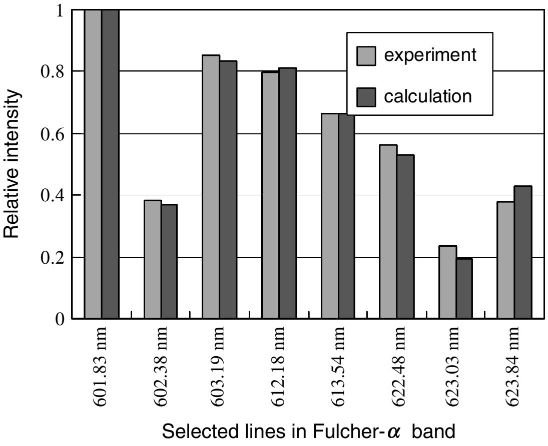

Fig. 2 Fulcher-α band line intensity fitting.

where the absence of primes denotes the ground state. Combining Eqs. (1) and (2), I is given by

$$I^{v',J'}_{v'',J''} = h\nu^{v',J'}_{v'',J''} A^{v',J'}_{v'',J''} \frac{N_e \sum_{v,J} N_{v,J} C^{v',J'}_{v,J}}{\sum_{v'',J''} A^{v',J'}_{v'',J''}} \tag{3}$$

Assuming the Boltzmann distribution at the ground state, $N_{v,J}$ is described as a function of rotational and vibrational temperatures at the ground state. $C^{v',J'}_{v,J}$ is a function of the electron temperature. The validity of the corona assumption was discussed in [15]. As a result, I in Eq. (3) can be described as a function of T_{rot}, T_{vib}, and T_e. We determined these three temperatures by intensity fitting of the selected eight lines. Figure 2 shows an example of this intensity fitting. The selected lines are tabulated in Table 1, in which $Q1$, for example, means Q branch (no change in rotational quantum number) and $J' = J'' = 1$. The calculated spectra agree well with the experimental data. Errors in T_{rot}, T_{vib}, and T_e were about 10, 30, and 40%, respectively [15], thus confirming that this method can be used to determine T_{rot} with good accuracy.

Table 1 Selected spectral lines (nanometers)

Transition ($v' - v''$)	Q1	Q2	Q3
0-0	601.83	602.38	603.19
1-1	612.18	——	613.54
2-2	622.48	623.03	623.84

III. Translational Temperature Determination Method

The T_{tra} was determined here using Doppler broadening of the Balmer H_β line. Various types of spectral line broadening were evaluated as follows, and the contribution of each factor was discussed.

A. Doppler Broadening

Doppler broadening is a broadening due to the random motion of particles of the emitting species. A Doppler broadened line has a Gaussian shape described as

$$f_{\mathrm{Doppler}}(\lambda) = \frac{1}{\sqrt{2\pi}\sigma_D}\exp\left[-\frac{(\lambda-\lambda_0)^2}{2\sigma_D^2}\right] \tag{4}$$

where λ_0 is the center wavelength. The full width at half-maximum (FWHM) of Doppler broadening is given by [18]:

$$\Delta\lambda_{\mathrm{Doppler}} = 2\sqrt{2\,\ell n\, 2}\sigma_D = 7.16\times10^{-7}\lambda_0\sqrt{\frac{T_{\mathrm{tra}}}{M}}\ \mathrm{nm} \tag{5}$$

Equation (5) shows that Doppler broadening decreases when M increases. Doppler broadening for the atomic hydrogen line is the largest among all atomic or molecular lines. For the H_β line, the FWHM of Doppler broadening can be expressed as

$$\Delta\lambda_{\mathrm{Doppler}} = 3.39\times10^{-4}\sqrt{T_{\mathrm{tra}}}\ \mathrm{nm} \tag{6}$$

B. Instrumental Broadening

Instrumental broadening was determined by using the atomic line of Xe at 482.9708 nm emitted from a calibration lamp. In our spectroscopic system, the instrumental function f_{inst} was given as

$$f_{\mathrm{inst}}(\lambda) = \begin{cases} \exp\left[-\frac{(\lambda-\lambda_0)^2}{2\sigma^2}\right] & |\lambda-\lambda_0| < 1.33506\times10^{-2}\ \mathrm{nm} \\ \frac{\alpha^2}{\alpha^2+(\lambda-\lambda_0)^2} & |\lambda-\lambda_0| > 1.33506\times10^{-2}\ \mathrm{nm} \end{cases} \tag{7}$$

where $\sigma = 6.795\times10^{-3}$ and $\alpha = 5.508\times10^{-3}$. Figure 3 shows f_{inst} fitted to the experimental data by the combination of Gaussian and Lorentzian profiles given by Eq. (7). FWHM of instrumental broadening was 0.016 nm.

C. Natural Broadening

Natural broadening is a broadening caused by the finite radiative lifetime of one or both energy levels involved in a transition. This uncertainty in the lifetime induces uncertainty in the energy, which in turn leads to spectral line broadening. FWHM of natural broadening is given as follows [19]:

$$\Delta\lambda_{\mathrm{natural}} = \frac{\lambda^2}{2\pi c}\left(\frac{1}{\tau_{n=4}}+\frac{1}{\tau_{n=2}}\right) \tag{8}$$

where τ is radiative lifetime, which can be calculated from transition probabilities [20]. For example, $\tau_{n=4}$ is the reciprocal of the summation of the transition probabilities for transitions from $n = 4$ to $n = 1$, 2, and 3, and thus, the calculated $\tau_{n=4}$ and $\tau_{n=2}$ are 3.31×10^{-8} and 2.13×10^{-9} s, respectively. Therefore, $\Delta\lambda_{\mathrm{natural}}$ of the H_β line is 6.27×10^{-5} nm.

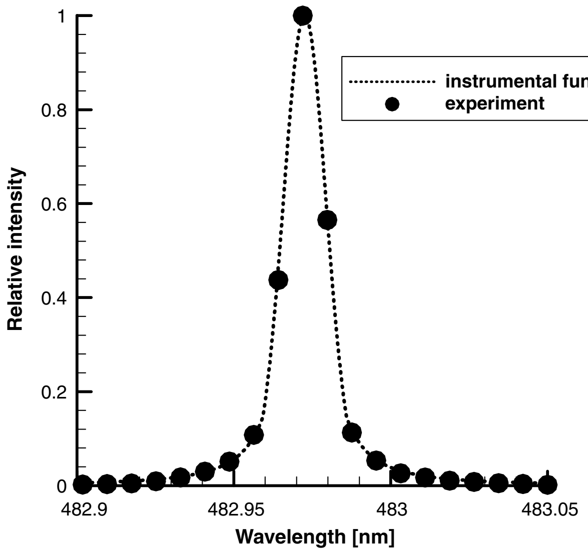

Fig. 3 Instrumental function.

D. Stark Effect

Stark broadening is a broadening caused by the splitting of spectral lines in an electric field. Under particular conditions, the Stark effect of the H_β line is the dominant mechanism in spectral broadening. The Stark profile has therefore been used as an accurate indicator of electron number density N_e [21–23]. The FWHM due to the Stark effect was tabulated by Touma et al. [24]. Although Stark broadening depends on both the N_e and T_e, its dependency on T_e is very weak. The influence of T_e on the Stark broadening is within a few percent, and therefore, without loss in accuracy, FWHM due to the Stark effect can be assumed to be a function only of N_e. Based on the table tabulated by Touma, FWHM due to the Stark effect $\Delta\lambda_{\mathrm{Stark}}$ can be approximated as

$$\log_{10}\Delta\lambda_{\mathrm{Stark}} = 0.686\log_{10}N_e - 15.13 \tag{9}$$

E. Zeeman Effect

Zeeman broadening is a broadening caused by the splitting of spectral lines due to an external magnetic field. The magnetic field breaks the degeneracy of m. The degenerated level splits into $2l+1$ levels, and causes the splitting of emission lines. The wavelength shift due to the Zeeman effect $\delta\lambda_z$ can be written as

$$\delta\lambda_z = \frac{\lambda^2}{c}\frac{\mu_B B}{h}(g_2 m_2 - g_1 m_1) \tag{10}$$

where subscripts 1 and 2 denote the lower and upper states, respectively. Lande g factor is given by [25]:

$$g \approx 1 + \frac{j(j+1)+s(s+1)-l(l+1)}{2j(j+1)} \tag{11}$$

Because the selection rule for m is that $\Delta m = 0, \pm1$, all possible wavelength shifts caused by the Zeeman effect can be calculated using Eq. (10).

F. Fine Structures

Degenerated energies are split by spin-orbit interaction. Such interaction produces seven components of the H_β line. These components, called fine structures, are listed in Table 2, where the relative intensity w_i of each component was calculated using the same method that Condon and Shortley used for the fine structures of an H_α line [26]. The H_β line profile observed by using a spectrometer is the sum of these seven components.

G. H_β Line Spectral Fitting Method

To calculate the H_β line observed by using the spectrometer, we first compare the contributions of Doppler, instrumental, natural, Stark, and Zeeman broadenings, and find the dominant contributing factors. The spectral profile for each fine structure can be calculated using only these dominant factors. Then, we superimpose the seven components of the fine structure using their relative intensities shown in Table 2.

The Zeeman effect can be neglected in our experiments because the maximum wavelength shift $\delta\lambda_{z,\max}$, calculated using Eq. (10) with the representative value of magnetic field strength shown in Sec. IV, $B = 42$ mT, is 6.2×10^{-4} nm. Figure 4 shows the FWHM

Table 2 Fine structures of the H_β line

Index	Upper state	Lower state	Wavelength, nm	Relative intensity, w_i
1	$4^2D_{5/2}$	$2^2P_{3/2}$	486.13614	288/9
2	$4^2D_{3/2}$	$2^2P_{3/2}$	486.13650	32/9
3	$4^2D_{3/2}$	$2^2P_{1/2}$	486.12785	160/9
4	$4^2P_{3/2}$	$2^2S_{1/2}$	486.12869	10
5	$4^2P_{1/2}$	$2^2S_{1/2}$	486.12977	5
6	$4^2S_{1/2}$	$2^2P_{3/2}$	486.13748	8/9
7	$4^2S_{1/2}$	$2^2P_{1/2}$	486.12883	4/9

of Doppler, instrumental, natural, and Stark broadenings. Stark broadening is a function of N_e. Doppler broadening is a function of T_{tra}, and Fig. 4 shows this broadening for a translational temperature $T_{\mathrm{tra}} = 500$ and 1000 K. These temperatures are chosen based on the experimental results shown in Sec. V. Natural broadening and instrumental broadening are independent of both N_e and T_{tra}. Figure 4 shows that the Stark broadening becomes less dominant when N_e decreases. Then, the range of N_e at which Stark broadening is negligible in comparison with Doppler broadening must be determined. The error caused by not considering Stark broadening can be estimated by comparing FWHM of only the Doppler profile $\Delta\lambda_{\mathrm{Doppler}}$ with that of the profile obtained by the convolution of Doppler and Stark profiles $\Delta\lambda_{\mathrm{Doppler+Stark}}$. The Holtzmark profile was used as the Stark profile [27]. Based on Eq. (6), the relative error in T_{tra} is described using the relative error in FWHM as follows:

$$\frac{T_{\mathrm{tra,Doppler+Stark}} - T_{\mathrm{tra,Doppler}}}{T_{\mathrm{tra,Doppler}}} = 2\frac{\Delta\lambda_{\mathrm{Doppler+Stark}} - \Delta\lambda_{\mathrm{Doppler}}}{\Delta\lambda_{\mathrm{Doppler}}} \tag{12}$$

As shown in Fig. 5, the relative error in T_{tra} in the range of 500–1000 K is within 3% when $N_e < 5 \times 10^{17}\ \mathrm{m}^{-3}$. In this range of N_e, the dominant contributing factors in the broadening of the H_β line shown in Fig. 4 are Doppler and instrumental broadenings.

Therefore, when $N_e < 5 \times 10^{17}\ \mathrm{m}^{-3}$, T_{tra} can be estimated within a 3% error using the following procedure:

1) Guess an approximate value for T_{tra}.

2) Convolve $f_{\mathrm{Doppler}}(\lambda)$ and $f_{\mathrm{inst}}(\lambda)$ for each of the seven components:

$$f_{d,i}(\lambda) = \int_0^\infty f_{\mathrm{Doppler}}(\lambda') f_{\mathrm{inst}}(\lambda - \lambda')\, \mathrm{d}\lambda' \tag{13}$$

3) Superimpose the contributions of the seven components:

$$f_{\mathrm{cal}}(\lambda) = \sum_{i=1}^{7} w_i f_{d,i}(\lambda) \tag{14}$$

4) Compare $f_{\mathrm{cal}}(\lambda)$ with experimental data $f_{\mathrm{exp}}(\lambda)$.

5) Repeat steps 1–4 for different T_{tra}, and finally determine the value of T_{tra} that best fits the experimental data.

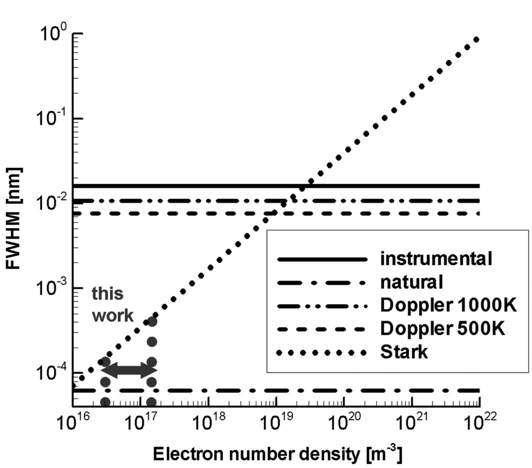

Fig. 4 Comparison between various contributing factors to H_β line broadening.

IV. Experimental Setup

Figure 6 shows a schematic of the plasma wind tunnel, which was developed to simulate the high-altitude flight of probes entering the atmosphere of outer planets [28]. Plasma was produced by using inductive heating at low pressure. The induced electric current, which was caused by temporal variation in a radio-frequency (RF) magnetic field, accelerated the electrons that collided with neutral particles and caused chemical reactions such as dissociation and ionization. As a result, a weakly ionized plasma consisting of H_2, H, H^+, and e^- was produced. A quartz tube with an inner/outer diameter of 46/50 mm was surrounded by four turns of a water-cooled coil. An RF power supply operating at a frequency of 13.56 MHz and maximum output power of 2 kW was connected to a matching network that cancels the power reflected from the plasma. An argon admixture (hydrogen admixed with a small amount of argon) was used as a test gas to measure the degree of dissociation by actinometry [15]. The gas was regulated by using a mass flow controller and injected through two opposing ports. Downstream of the RF coil was a direct current (dc) coil connected to a dc power supply that had a maximum current of 256 A. This dc coil was made by wrapping 3-mm-diam copper tube around the quartz tube. The copper tube was cooled by water flowing through the tube, and each turn was insulated by thermal shrinking tube. This dc coil generated a dc convergent–divergent magnetic field that squeezed and compressed the plasma flow to the center line, thus decreasing the heat loss to the wall of the quartz tube [29]. An orifice plate (orifice diameter of 12 mm and plate thickness of 5 mm) was installed at the downstream end of the quartz tube. At this orifice, the plasma flow was exhausted as a sonic jet and accelerated to supersonic speed by expansion in the test section. The combination of the dc magnetic field and the orifice plate converted the plasma source generated by

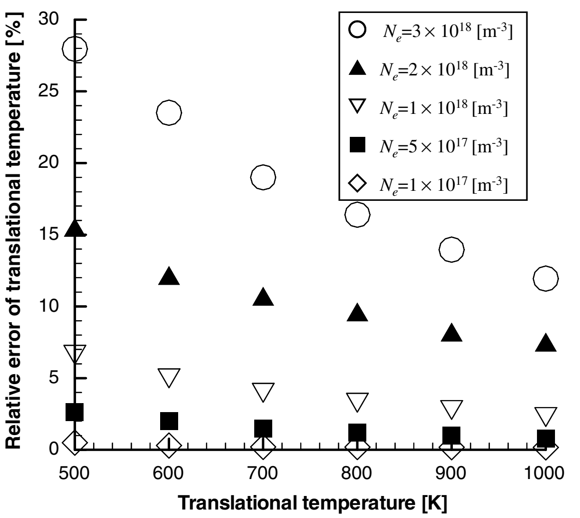

Fig. 5 Relative error in translational temperature by Stark broadening.

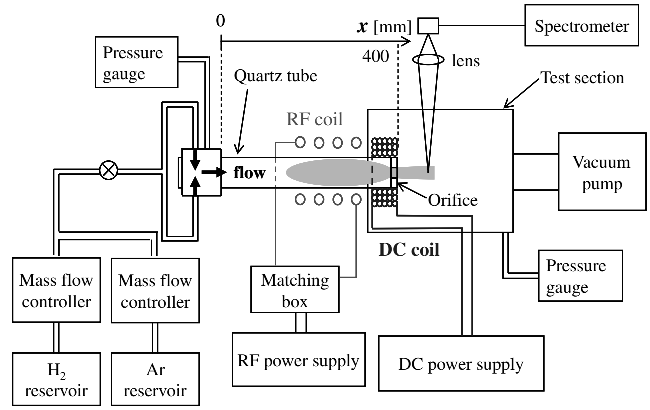

Fig. 6 Experimental apparatus.

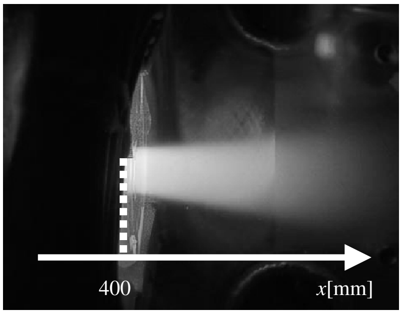

Fig. 7 Hydrogen plasma flow.

the RF coil into a supersonic plasma jet. Figure 7 shows a photo of the generated hydrogen plasma supersonic jet. The dashed line is just at the orifice exit (position $x = 400$ mm; see Fig. 6 for the coordinate system).

Table 3 summarizes the experimental condition. The reservoir pressure was measured at the static port on the orifice plate, because the flow upstream of the orifice is quite slow and thus considered at the reservoir condition. The pitot pressure was measured at $x = 430$ mm downstream of the orifice. Using the normal shock wave relation to the total pressure, the flow Mach number was calculated as 2.5 ± 0.2 at $x = 430$ mm, assuming γ is $\frac{5}{3}$, the same as that of monatomic gases. The use of the normal shock wave relation might not be valid in nonequilibrium or rarefied flow. However, as described in Sec. V, the internal energy modes were almost frozen in the plasma flows studied here, and thus did not contribute to the shock wave relationship. Although the effect of rarefied flow was not taken into account in the normal shock wave relation, the difference between the measured pitot pressure (30 Pa) and the numerically calculated pitot pressure obtained by Sec. V (36 Pa) was 20%. Therefore, for simplicity, the normal shock wave relation was used as an approximation.

The pitot tube in this study had an inner/outer diameter of 4/6 mm. This large inner-diameter pitot tube was used because the response of a pitot tube in low-pressure flow is slow, and thus reaching steady state would take considerable time with a smaller inner-diameter pitot tube. The local static pressure was calculated from the stagnation pressure and the local Mach number. Based on the orifice diameter and measured T_{tra} (see Sec. V), the calculated Knudsen number was 0.62. Therefore, the plasma flow used in this study could be categorized as transitional flow [30].

Table 3 Experimental condition

Mass flow rate, H_2	0.3	SLM
Mass flow rate, Ar	0.03	SLM
Input RF power	1.0	kW
Dc coil current	50	A
Dc magnetic field flux at the center of dc coil	42	mT
Average specific enthalpy	320	MJ/kg
Stagnation pressure	55	Pa
Static pressure at $x = 430$ mm	3.3	Pa
Mach number at $x = 430$ mm	2.5	——
Flow velocity at $x = 430$ mm	2.8×10^3	m/s
Knudsen number for orifice diameter	0.62	——

Figure 6 also shows the optical system in the emission spectroscopic method. The measurement point was determined by the lens system installed in front of the spectrometer. The emission focused by the lens was directed into the spectrometer (Hamamatsu, PMA-50) through an optical fiber. The spot size of the detected emission at the measurement point was 2 mm. Two gratings were used: one for T_{tra} and the other for T_{rot} (Table 4). The exposure time for a single sample depended on emission intensity at the measurement point. During all measurements, time variation in the emission intensity was within ±3%, indicating stable plasma flow. The measured data were obtained by averaging 4–10 samples.

V. Results and Discussion

The emission spectroscopic method to determine T_{tra} and T_{rot} described in Secs. II and III was applied to the experimental apparatus described in Sec. IV. Variations in T_{rot}, T_{vib}, and T_e in the radial direction in the freestream were found to be within 20% by using Abel inversion [31], indicating radial uniformity in the freestream. In addition, $T_{\mathrm{vib}} = 2000$ K and $T_e = 22,000$ K and were uniform also in the axial direction. In this section, first, estimation of N_e is described. The result suggests that Stark effect was negligible in our experiments, and thus the T_{tra} determination method (Sec. III) could be applied. Then, measurement of T_{tra} and T_{rot} along the centerline for flow passing a blunt body is described. The measured distributions of T_{tra} and T_{rot} seemed reasonable compared with the translational–rotational relaxation time reported in the literature and with results obtained using numerical simulation.

A. Estimation of Electron Number Density

To clarify the effect of Stark broadening on the entire spectral broadening, N_e must be estimated. To accurately predict N_e, a computational code that considers the plasma generation section in the quartz tube and the test section is necessary, but time consuming to develop. Because determining whether Doppler broadening is dominant compared with Stark broadening requires only knowing the order of magnitude of N_e, a method to estimate N_e using a simple model was developed and applied here as follows.

Figure 8 schematically shows the simple one-dimensional flow approximation. In this approximation, only H_2 and Ar enter the inlet. As a result of inductive heating, H_2, H, H^+, Ar, Ar^+, and e^- are exhausted from the exit. At the inlet, the gas is assumed to be almost still. The pressure, T_{tra}, and degree of dissociation at $x = 430$ mm were used as the exit condition. No velocity slip among heavy particles is also assumed. The number density of hydrogen atoms can be calculated by measuring the degree of dissociation by using actinometry [15]. The degree of dissociation was calculated from the intensity ratio of the Balmer H_β line to that of the Ar 750.4 nm line. Figure 9 shows the degree of dissociation along the centerline determined without Abel inversion. The error bars were calculated by considering the uncertainties in T_e and in the excitation cross section data [15]. The degree of dissociation was about 2–8% and decreased downstream.

Table 4 Gratings used to measure translational temperature and rotational temperature

Measured temperature		T_{tra}	T_{rot}
Number of grooves	gr/mm	3600	600
Measurement resolution	nm	0.0078	0.08
Wavelength width observed for a single data sampling	nm	7.98	82
Exposure time	ms	20–1000	200–2000

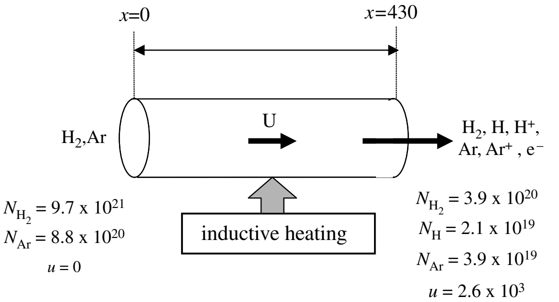

Fig. 8 Simple one-dimensional model.

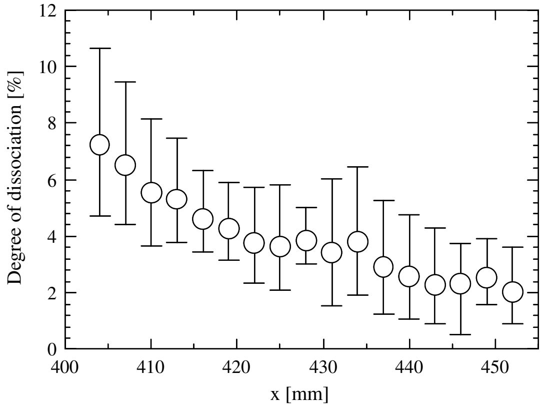

Fig. 9 Degree of dissociation.

Assuming that the chemical reactions caused by the electron impact were dominant in our plasma and that no backward reactions occurred, we consider only the following chemical reactions:

$$H_2 + e^- \rightarrow 2H + e^-$$

$$H + e^- \rightarrow H^+ + 2e^-$$

$$Ar + e^- \rightarrow Ar^+ + 2e^-$$

Using the approximation of steady flow without diffusion, the conservation laws of chemical species H and e^- can be described as

$$\frac{d}{dx}(N_H u) = 2k_d N_{H_2} N_e - k_{i1} N_H N_e \tag{15}$$

$$\frac{d}{dx}(N_e u) = k_{i1} N_H N_e + k_{i2} N_{Ar} N_e \tag{16}$$

The controlling temperature in the rate coefficients is T_e, because both dissociation and ionization reactions are governed by the electron energy. To take the uncertainty in these rate constants into account, we used two different k_d [5,32], two k_{i1} [5,33], and three k_{i2} [34–36].

The order of each term in Eqs. (15) and (16) can be estimated using characteristic velocity U and characteristic length L. Equations (13) and (14) can then be rewritten as

$$\frac{N_{H,av} U}{L} = 2k_d N_{H_2 av} N_{e,av} - k_{i1} N_{H,av} N_{e,av} \tag{17}$$

$$\frac{N_{e,av} U}{L} = k_{i1} N_{H,av} N_{e,av} + k_{i2} N_{Ar,av} N_{e,av} \tag{18}$$

The subscript av means the average value between the inlet and exit. Using Eqs. (17) and (18), the average N_e can be estimated as

$$N_{e,av} = \frac{k_{i1} N_{H,av} + k_{i2} N_{Ar,av}}{2k_d N_{H_2,av} - k_{i1} N_{H,av}} N_{H,av} \tag{19}$$

Because we assume no electrons at the inlet, N_e at the exit can be estimated as

$$N_{e,exit} = 2N_{e,av} = 2.8 \times 10^{16} - 1.3 \times 10^{17}\ m^{-3} \tag{20}$$

Therefore, in our experiments, the estimated N_e was less than $5 \times 10^{17}\ m^{-3}$. The validity of our assumption that electron impact dissociation and ionization are dominant can be easily confirmed using the rate coefficients of dissociation and ionization reactions caused by collisions with heavy particles [37,38]. The other assumption of no backward reactions was also confirmed by comparing the forward reaction rates with the backward reaction rates [34,37]. Consequently, from Fig. 4, we can neglect the Stark effect and thus estimate T_{tra} using the method described in Sec. III.

B. Translational–Rotational Nonequilibrium of Flow Behind a Shock Wave

As shown in Fig. 10, a blunt body (nose radius of 3 mm) was put in the plasma wind tunnel, and the translational–rotational nonequilibrium behind a shock wave was investigated using our emission spectroscopic method. The position $x = 430$ mm was the nose tip of the body. The measurement was done every 1 mm near the nose tip. The data shown here were measurements only along the centerline in the axial direction, and Abel inversion was not done. Figure 11 shows a representative H_β line profile fitting for determining T_{tra}. The line calculated by using our emission spectroscopic method reproduced the experimental data well. Figure 12 shows the comparison between the measured T_{tra} and T_{rot}. Two types of bars are shown in Fig. 12. The thin vertical bars show the sensitivity, which indicates the possible changes in the absolute values of the temperatures, but no significant changes in the shape of the temperature profile. The thin bar for T_{rot} indicates the sensitivity of T_{rot} considering the fitting error was 5%. The thin bar for T_{tra} was determined by considering the fitting error in the instrumental

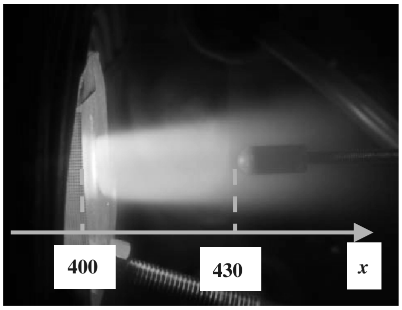

Fig. 10 Blunt body in the plasma wind tunnel.

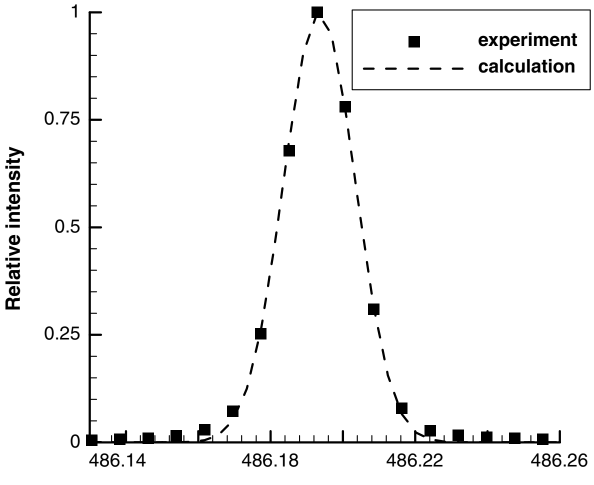

Fig. 11 Fitting example of H_β line.

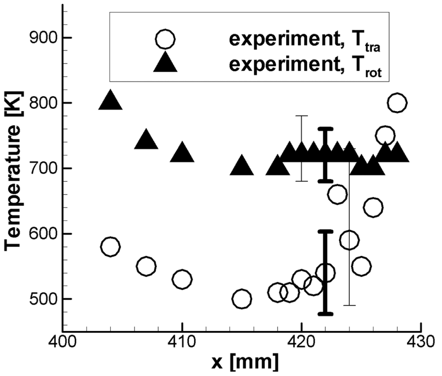

Fig. 12 Translational temperature and rotational temperature in front of a blunt body.

function. In contrast to the thin bars indicating sensitivity, the thick bars indicate variations in the five experiments and confirm good repeatability in the measurements.

As the result of the emission spectroscopy at the plasma generation part near the RF coil, both T_{tra} and T_{rot} were around 1700 K, indicating thermal equilibrium between translational and rotational modes. However, their nonequilibrium occurred due to the strong free expansion at the orifice exit; T_{tra} rapidly decreased at the exit, whereas T_{rot} gradually decreased due to the relaxation process. This type of nonequilibrium phenomena is often seen in nonequilibrium nozzle flows [39–41].

In front of the nose tip (at $x = 430$ mm), only T_{tra} increased from 500 to 850 K. Because our plasma flow was supersonic, this increase in T_{tra} suggests the presence of a shock wave. The gradual increase was because the plasma flow was rarefied. In rarefied flows, a shock wave cannot be observed as a discontinuity. The increase in T_{tra} in the experiments in our study was smaller than that calculated from the normal shock wave relation; according to the normal shock wave relation using a Mach number of 2.5, T_{tra} must increase by a factor of 2.1 after the normal shock wave. This discrepancy between measured and calculated increase in T_{tra} might be caused by several factors:

1) The shock wave has thickness because of the rarefied flow.

2) Determining the Mach number by using the pitot tube pressure in rarefied flow might not be valid.

3) Determination of the value of γ is difficult in nonequilibrium flow.

4) Light diffraction near the body causes measurement error.

The translational–rotational nonequilibrium can be checked by comparing τ_f with τ_r. Assuming the normal shock wave in front of the body, the flow velocity behind the shock wave U_{after} was 1.1×10^3 m/s. Taking a characteristic length L as 10 mm, where T_{tra} was increasing, τ_f can be calculated as

$$\tau_f = \frac{L}{U_{\mathrm{after}}} = 9.5 \times 10^{-6}\ \mathrm{s} \tag{21}$$

In a T_{tra} range of 600–900 K, τ_r can be estimated as 9.3×10^{-5} to 1.3×10^{-4} s [42]. The static pressure was calculated based on the normal shock wave relation. Because τ_f is smaller than τ_r, translational and rotational modes should be in nonequilibrium. This is consistent with the experimental results shown in Fig. 12, thus confirming that our emission spectroscopic method could be used to successfully observe the nonequilibrium between translational and rotational modes.

Finally, we compared the experimental results with numerical simulation results. Because of the rarefied flow, we used the direct simulation Monte Carlo (DSMC) method. Our numerical code calculates the three-dimensional thermal nonequilibrium flow, with the variable hard sphere model. For energy exchange in inelastic collisions, we used the Larsen–Borgnakke model [43]. The average probabilities of translational–rotational and translational–vibrational energy exchange for H_2-H_2 collisions are given by Boyd [5]. Chemical reactions were assumed to be frozen. The temperature of the body wall was 300 K, and sample particles were assumed to diffusively reflect on the wall. The convergence of DSMC simulation was checked for the cell size, the number of sample particles, and the time step. The variation in the peak T_{tra} was within 2%.

Figures 13 and 14, respectively, show the axial distributions of T_{tra} and T_{rot} calculated using the DSMC method. Note that this comparison is qualitative, not quantitative, because the experimental and computational conditions are not exactly the same. In the experiment, the plasma flow strongly expanded after the orifice and accelerated downstream. In contrast, in the DSMC simulation, the uniform freestream at Mach number 2.5 comes to the body. The thick lines in Figs. 13 and 14 show the DSMC-calculated temperature distributions on the symmetric axis, and the thin lines show the DSMC-calculated temperature distributions averaged in the radial direction as follows:

$$T_{\mathrm{av}} = \frac{1}{r_p} \int_0^{r_p} T(r)\,\mathrm{d}r \tag{22}$$

where r_p is the plasma radius. The experimental data should be compared with the region between the thick and thin lines because 1) an Abel inversion was not done for the experimental data, and the spectrometer detected the integral of the emission in the radial direction, and 2) the temperature profile in the radial direction could be directly obtained in the DSMC calculation. Figures 13 and 14 show similar tendencies, namely, a gradual increase in T_{tra} and a relatively constant T_{rot}. T_{tra} begins to rise due to the shock wave at almost the same location. The maximum T_{tra} obtained using the DSMC method is similar to that obtained experimentally. Qualitatively, the experimental results and the numerical simulation results agree well, and the gradual increase in T_{tra} in the rarefied shock layer was successfully observed.

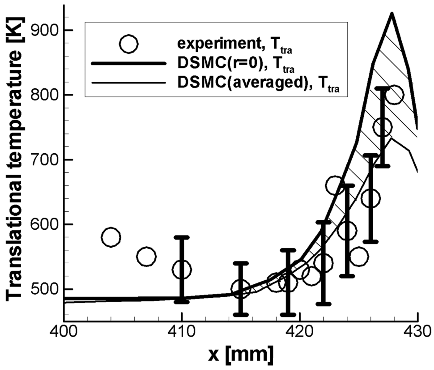

Fig. 13 Comparison between experimental and DSMC-calculated translational temperature.

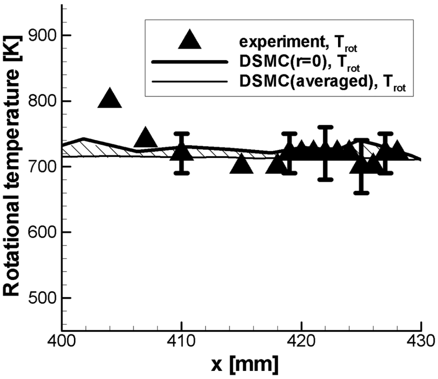

Fig. 14 Comparison between experimental and DSMC-calculated rotational temperature.

VI. Conclusions

In this study, translational–rotational nonequilibrium in low-density hydrogen plasma flow was examined. A method to determine translational and rotational temperatures by emission spectroscopy was presented. Based on the estimation of each factor contributing to H_β line broadening, the translational temperature in plasma that has low electron number density less than 5×10^{17} m^{-3} can be determined by H_β line profile fitting, taking into account instrumental broadening, Doppler broadening, and spin-orbit coupling. Line intensity fitting of the Fulcher-α band was used to determine the rotational temperature. Finally, by applying this emission spectroscopic method, we experimentally studied the translational–rotational relaxation in hydrogen plasma flow passing the blunt body. Only translational temperature increased in front of the nose, and rotational temperature was almost constant. This nonequilibrium between translational and rotational modes can be reasonably explained by comparing the translational–rotational relaxation time in the literature with the flow characteristic time. Because our plasma flow was rarefied, the translational temperature gradually increased, which was qualitatively confirmed by the DSMC simulation.

Acknowledgments

This work was supported by Grant-in-Aid for Scientific Research No. 18.11672, No. 17360408, and No. 21360413 of the Japan Society for the Promotion of Science. The first author is supported by Research Fellowships of the Japan Society for the Promotion of Science for Young Scientists.

References

[1] Vincenti, W. R., and Kruger, C. H., Jr., *Introduction to Physical Gas Dynamics*, Krieger, Malabar, FL, 1967, p. 197.

[2] Bird, G. A., *Molecular Gas Dynamics and the Direct Simulation of Gas Flows*, Clarendon, Oxford, England, U.K., 1994, pp. 413–414.

[3] Parker, J. G., "Rotational and Vibrational Relaxation in Diatomic Gases," *Physics of Fluids*, Vol. 2, No. 4, 1959, pp. 449–462. doi:10.1063/1.1724417

[4] Gnoffo, P. A., Gupta, R. N., and Shinn, J. L., "Conservation Equations and Physical Models for Hypersonic Air Flows in Thermal and Chemical Nonequilibrium," NASA TP 2867, 1989, p. 10.

[5] Boyd, I. D., "Monte Carlo Simulation of Nonequilibrium Flow in a Low-Power Hydrogen Arcjet," *Physics of Fluids*, Vol. 9, No. 10, 1997, pp. 3086–3095. doi:10.1063/1.869474

[6] Gallagher, R. J., and Fenn, J. B., "Rotational Relaxation of Molecular Hydrogen," *Journal of Chemical Physics*, Vol. 60, No. 9, 1974, pp. 3492–3499. doi:10.1063/1.1681565

[7] Boyd, I. D., Beattie, D. R., and Cappelli, M. A., "Numerical and Experimental Investigations of Low-Density Supersonic Jets of Hydrogen," *Journal of Fluid Mechanics*, Vol. 280, No. 1, 1994, pp. 41–67. doi:10.1017/S0022112094002843

[8] Winter, T. G., and Hill, G. L., "High-Temperature Ultrasonic Measurements of Rotational Relaxation in Hydrogen, Deuterium, Nitrogen, and Oxygen," *Journal of the Acoustical Society of America*, Vol. 42, No. 4, 1967, pp. 848–858. doi:10.1121/1.1910657

[9] Lordi, J. A., and Mates, R. E., "Rotational Relaxation in Nonpolar Diatomic Gases," *Physics of Fluids*, Vol. 13, No. 2, 1970, pp. 291–308. doi:10.1063/1.1692920

[10] Vivien, C., Hermann, J., Perrone, A., Boulmer-Leborge, C., and Luches, A., "A Study of Molecule Formation During Laser Ablation of Graphite in Low-Pressure Nitrogen," *Journal of Physics D: Applied Physics*, Vol. 31, No. 10, 1998, pp. 1263–1272. doi:10.1088/0022-3727/31/10/019

[11] Matsuda, A., Fujita, K., Sato, S., and Abe, T., "Nonequilibrium Phenomena Behind Strong Shock Waves Generated in Superorbital Reentry Flight," *Journal of Thermophysics and Heat Transfer*, Vol. 18, No. 3, 2004, pp. 342–348. doi:10.2514/1.6244

[12] Chu, H. N., Hartog, E. A., Lefkow, A. R., Jacobs, J., Anderson, L. W., Lagally, M. G., and Lawler, J. E., "Measurements of the Gas Kinetic Temperature in a CH_4-H_2 Discharge During the Growth of Diamond," *Physical Review A: General Physics*, Vol. 44, No. 6, 1991, pp. 3796–3803. doi:10.1103/PhysRevA.44.3796

[13] Qing, Z., Otorbaev, D. K., Brussaard, G. J. H., van der Sanden, M. C. M., and Schram, D. C., "Diagnostics of the Magnetized Low-Pressure Hydrogen Plasma Jet: Molecular Regime," *Journal of Applied Physics*, Vol. 80, No. 3., 1996, pp. 1312–1324. doi:10.1063/1.362930

[14] Rutkowski, M., Wetzig, D., and Zacharias, H., "Rotational and Vibrational Population of D_2 Desorbing from Sulfur-Covered Pd (100)," *Physical Review B: Solid State*, Vol. 66, No. 11, 2002, p. 115405. doi:10.1103/PhysRevB.66.115405

[15] Takama, Y., and Suzuki, K., "Spectroscopic Diagnostics of Thermochemical Nonequilibrium Hydrogen Plasma Flow," *Journal of Thermophysics and Heat Transfer*, Vol. 21, No. 3, 2007, pp. 630–637. doi:10.2514/1.28288

[16] Alsmeyer, H., "Density Profiles in Argon and Nitrogen Shock Waves Measured by the Absorption of an Electron," *Journal of Fluid Mechanics*, Vol. 74, No. 3, 1976, pp. 497–513. doi:10.1017/S0022112076001912

[17] Robben, F., and Talbot, L., "Measurement of Shock Wave Thickness by the Electron Beam Fluorescence Method," *Physics of Fluids*, Vol. 9, No. 4, 1966, pp. 633–643. doi:10.1063/1.1761728

[18] Cowan, R. D., *The Theory of Atomic Structure and Spectra*, Univ. of California Press, Berkeley, CA, 1981, p. 20.

[19] Cowan, R. D., *The Theory of Atomic Structure and Spectra*, Univ. of California Press, Berkeley, 1981, pp. 18–19.

[20] Wiese, W. L., Smith, M. W., and Glennon, B. M., *Atomic Transition Probabilities, Volume I: Hydrogen Through Neon*, U.S. Dept. of Commerce, National Bureau of Standards, 1966, pp. 2–6.

[21] Acon, B. W., Stehle, C., Zhang, H., and Montaser, A., "Stark-Broadened Hydrogen Line Profiles Predicted by the Model Microfield Method for Calculating Electron Number Densities," *Spectrochimica Acta Part B: Atomic Spectroscopy*, Vol. 56, No. 5, May 2001, pp. 527–539. doi:10.1016/S0584-8547(01)00201-4

[22] Zikic, R., Gigosos, M. A., Ivkovic, M., Gonzalez, M. A., and Konjevic, N., "A Program for the Evaluation of Electron Number Density from Experimental Hydrogen Balmer Beta Line Profiles," *Spectrochimica Acta Part B: Atomic Spectroscopy*, Vol. 57, No. 5, 2002, pp. 987–998. doi:10.1016/S0584-8547(02)00015-0

[23] Fujita, K., Sato, S., Abe, T., and Otsu, H., "Electron Density Measurements Behind Strong Shock Waves by H-β Profile Matching," *Journal of Thermophysics and Heat Transfer*, Vol. 17, No. 2, 2003, pp. 210–216. doi:10.2514/2.6753

[24] Touma, J. E., Oks, E., Alexiou, S., and Derevianko, A., "Review of the Advanced Generalized Theory for Stark Broadening of Hydrogen Lines in Plasmas with Tables," *Journal of Quantitative Spectroscopy and Radiative Transfer*, Vol. 65, Nos. 1–3, 2000, pp. 543–571. doi:10.1016/S0022-4073(99)00095-3

[25] Cowan, R. D., *The Theory of Atomic Structure and Spectra*, Univ. of California Press, Berkeley, CA, 1981, p. 487.

[26] Condon, E. U., and Shortley, G. H., *The Theory of Atomic Spectra*, Cambridge Univ. Press, Cambridge, England, U.K., 1959, pp. 69, 99, 132–134.

[27] Griem, H. R., *Plasma Spectroscopy*, McGraw–Hill, New York, 1964, pp. 72–78, 448.

[28] Nakamura, K., and Suzuki, K., "Aerothermodynamic Analysis on Low-Ballistic-Coefficient Aerocapture Vehicle with Membrane Decelerator," International Astronautical Congress Paper 05-E2.2.03, 2005.

[29] Takama. Y., and Suzuki, K., "Experimental Studies on Nonequilibrium Plasma Flow in a Convergent–Divergent Magnetic Field," *Plasma Sources Science and Technology*, Vol. 17, No. 1, 2008, p. 015005. doi:10.1088/0963-0252/17/1/015005

[30] Tsien, H. S., "Superaerodynamics, Mechanics of Rarefied Gases," *Journal of the Aeronautical Sciences*, Vol. 13, No. 12, 1946, pp. 653–664.

[31] Cremers, C. J., and Birkebak, R. C., "Application of the Abel Integral Equation to Spectrographic Data," *Applied Optics*, Vol. 5, No. 6, 1966, pp. 1057–1064. doi:10.1364/AO.5.001057

[32] Rubin, Y., Murphy, A. B., and Ishigaki, T., "Numerical Modeling of an Ar-H2 Radio-Frequency Plasma Reactor Under Thermal and Chemical

Nonequilibrium Conditions," *Plasma Chemistry and Plasma Processing*, Vol. 27, No. 2, 2007, pp. 189–204.
doi:10.1007/s11090-007-9055-5

[33] Park, J. H., Pfender, E., and Chang, C. H., "Reduction of Chemical Reactions in Nitrogen and Nitrogen-Hydrogen Plasma Jets Flowing into Atmospheric Air," *Plasma Chemistry and Plasma Processing*, Vol. 20, No. 2, 2000, pp. 165–181.
doi:10.1023/A:1007087105887

[34] Hoffert, M. I., and Lien, "Quasi-One-Dimensional, Nonequilibrium Gas Dynamics of Partially Ionized Two-Temperature Argon," *Physics of Fluids*, Vol. 10, No. 8, 1967, pp. 1769–1777.
doi:10.1063/1.1762356

[35] Bukowski, J. D., and Graves, D. B., "Two-Dimensional Fluid Model of an Inductively Coupled Plasma with Comparison to Experimental Spatial Profiles," *Journal of Applied Physics*, Vol. 80, No. 5, 1996, pp. 2614–2623.
doi:10.1063/1.363169

[36] Ma, J., and Pu, Y.-K., "Tuning the Electron Temperature of a Nitrogen Plasma by Adding Helium and Argon," *Physics of Plasmas*, Vol. 10, No. 10, 2003, pp. 4118–4122.
doi:10.1063/1.1605950

[37] Park, C., Laffe, R. L., and Partridge, H., "Chemical-Kinetic Parameters of Hyperbolic Earth Entry," *Journal of Thermophysics and Heat Transfer*, Vol. 15, No. 1, 2001, pp. 76–90.
doi:10.2514/2.6582

[38] McCay, T. D., and Dexter, C. E., "Chemical Kinetic Performance Losses for Hydrogen Laser Thermal Thruster," *Journal of Spacecraft and Rockets*, Vol. 24, No. 4, 1987, pp. 372–376.
doi:10.2514/3.25927

[39] Tirumalesa, D., "Nozzle Flows with Coupled Vibrational and Dissociational Nonequilibrium," *AIAA Journal*, Vol. 5, No. 2, 1967, pp. 254–260.
doi:10.2514/3.3950

[40] Bourdon, A., Leroux, A., Domingo, P., and Vervisch, P., "Experiment-Modeling Comparison in a Nonequilibrium Supersonic Air Nozzle Flow," *Journal of Thermophysics and Heat Transfer*, Vol. 13, No. 1, 1999, pp. 68–75.
doi:10.2514/2.6402

[41] Abe, K., Kameyama, T., Kihara, H., Nishida, M., Ito, K., and Tanno, H., "Computation and Experiment of Nonequilibrium Nozzle Flow of Arc-Heated Air," *Journal of Thermophysics and Heat Transfer*, Vol. 19, No. 4, 2005, pp. 428–434.
doi:10.2514/1.13603

[42] Billing, G. D., "Rotational and Vibrational Relaxation of Hydrogen and Deuterium," *Chemical Physics*, Vol. 20, No. 1, 1977, pp. 35–42.
doi:10.1016/0301-0104(77)85111-2

[43] Borgnakke, C., and Larsen, P. S., "Statistical Collision Model for Monte Carlo Simulation of Polyatomic Gas Mixture," *Journal of Computational Physics*, Vol. 18, No. 4, 1975, pp. 405–420.
doi:10.1016/0021-9991(75)90094-7